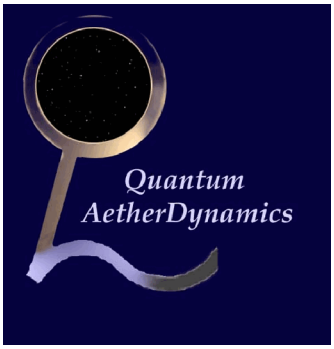

Quantum AetherDynamics Institute (QADI)

Quantum Illumination Density (qild): Wavelength-Projected Photomagnetic Activation in Laser-Plasma Coupling

David W. Thomson III
Quantum AetherDynamics Institute (QADI), Alma, Illinois, USA
ORCID: 0000-0002-5830-5427

Version 1.1 – June 25, 2026

This article is published by the Quantum AetherDynamics Institute (QADI).

It develops the Aether Physics Model (APM)

Abstract

This paper continues the QMU laser-plasma series by introducing Quantum Illumination Density, qild, as the characteristic-length projection of Quantum Photomagnetic Density, qpmd. In the preceding paper, qpmd was defined by

$$\mathrm{qpmd} = \frac{\mathrm{mchg}}{\mathrm{ligt}},$$

where

$$\mathrm{mchg} = m_{\mathrm{e}}\mathrm{mcaf} = \frac{m_{\mathrm{e}}}{{e_{\mathrm{emax}}}^2}, \qquad \mathrm{mcaf} = \frac{1}{{e_{\mathrm{emax}}}^2}.$$

Thus mchg is the mass-to-magnetic-charge ratio, not magnetic charge affinity itself. At the quantum luminous condition, the mass factor in mchg cancels the mass factor in ligt_q, giving

$$\mathrm{qpmd} = \frac{1}{{e_{\mathrm{emax}}}^2 {\lambda_C}^3 {F_q}^3}.$$

The present paper asks what quantity is measured when that photomagnetic activation density is projected through a characteristic length. The proposed QMU relation is

$$\mathrm{qild} = \lambda_C\,\mathrm{qpmd} = \frac{1}{{e_{\mathrm{emax}}}^2 {\lambda_C}^2 {F_q}^3},$$

where λ_C is the electron Compton length. The definition of quantum illumination density is constructed directly from the previously established photomagnetic activation density coordinate Thomson [2026]. This construction distinguishes transported photon quanta,

$$\mathrm{phtn},$$

from the local luminous state,

$$\mathrm{ligt} = \mathrm{phtn}\,\mathrm{freq},$$

and from illumination density,

$$\mathrm{qild},$$

which is interpreted as the characteristic-length projection of photomagnetic activation. The present treatment follows the QMU interpretation of luminous propagation and thermal organization developed previously in the Aether Physics Model literature Thomson III [2024].

The investigation uses an expanded hot-electron database derived from the Rusby et al. review and associated workbook, containing 555 usable records from electron measurements, x-ray measurements, simulations, and supplemental entries. The QMU regime coordinate

$$\eta_q = \Theta_e = \frac{E_h}{m_{\mathrm{e}}\,c^2}$$

is treated as the predicted quantity rather than merely as a diagnostic. Electron rest-energy normalization employs the CODATA 2022 recommended fundamental constants Tiesinga et al. [2023]. A forward QMU model is then tested:

$$\eta_{q,\mathrm{pred}} = A\left(I_{18}\lambda_L^2\right)^p \left(\frac{c\tau_L}{\lambda_L}\right)^s \left(\frac{L_p}{\lambda_L}\right)^r.$$

The leading dependence on the wavelength-projected intensity coordinate is consistent with the long-established relativistic scaling behavior of laser-plasma interactions Wilks et al. [1992, 2001], Kruer [1988]. The model uses wavelength-projected intensity, pulse duration in optical cycles, and pre-plasma scale length in laser wavelengths. Using five-fold cross-validation in logarithmic space, the full model reaches $R^2_{\log} = 0.829$ for all rows where the full model is available, $R^2_{\log} = 0.759$ for electron measurements, and $R^2_{\log} = 0.908$ for simulations. The fitted global intensity exponent is $p = 0.508959 \pm 0.014148$, close to square-root response in $I_{18}\lambda_L^2$. These results support a genuine QMU validation path: QMU-native coordinates can reproduce measured hot-electron structure from laser-plasma input parameters without using measured hot-electron temperature as an input.

1 Purpose and Research Question

The present investigation directly extends the previous demonstration of photomagnetic activation density (qpmd) as a QMU-derived diagnostic coordinate in laser-plasma data Thomson [2026]. That work used published hot-electron data to show that experimentally measured laser-solid interactions already contain the quantities required to compute a QMU activation coordinate. High-intensity laser–solid interactions produce hot-electron populations whose temperatures depend on laser wavelength, intensity, interaction geometry, and plasma conditions Wilks et al. [1992], Kruer [1988], Rusby et al. [2024].

The present paper continues that program. It asks:

> What physical quantity is being measured when photomagnetic activation density is projected through a wavelength?

The working hypothesis is:

> qpmd quantifies mass-to-magnetic-charge activation per luminous condition,

whereas

> qild quantifies the characteristic-length projection of that activation.

The objective is not to compete against existing laser-plasma scaling laws. The objective is QMU validation. The question is whether QMU-derived coordinates can reproduce the measured organization already present in the data.

Table 1: QMU coordinates used in this paper.

Coordinate	Definition	Operational meaning
phtn	transported photon quantum	photon transport into the target region
ligt	phtn freq	local luminous state established by photon-frequency action
Θ_e	$E_h/(m_{\mathrm{e}}\,c^2)$	electron rest-energy fraction measured from hot-electron energy
η_q	Θ_e	QMU illumination-regime coordinate to be predicted
q_T^*	$\Theta_e\lambda_L$	practical wavelength-projected thermal activation coordinate
qpmd	mchg/ligt	mass-to-magnetic-charge activation per luminous condition
qild	λ_C qpmd	characteristic-length projection of photomagnetic activation

2 Photon Quanta, Luminous State, and Illumination Density

In the QMU framework, transported photon quanta are represented as

$$\text{phtn}.$$

The local luminous state is represented as

$$\text{ligt} = \text{phtn}\,\text{freq}.$$

This distinction is important for laser-plasma analysis. The laser pulse transports photon quanta, but the target plasma responds to the luminous state established locally by those photons. Electron heating, self-generated magnetic fields, x-ray production, and ion acceleration therefore measure the organization of a luminous coupling condition rather than photon count alone.

Quantum illumination density is defined as

$$\text{qild} = \lambda_C\,\text{qpmd}.$$

Thus qpmd remains the volumetric photomagnetic activation coordinate,

$$\text{qpmd} = \frac{1}{{e_{\text{emax}}}^2 {\lambda_C}^3 {F_q}^3},$$

while qild is its characteristic-length projection,

$$\text{qild} = \frac{1}{{e_{\text{emax}}}^2 {\lambda_C}^2 {F_q}^3}.$$

The use of λ_C is not an arbitrary scale insertion. The measured response in this paper is the hot-electron sector. The electron rest energy defines

$$\Theta_e = \frac{E_h}{m_{\text{e}}\,c^2},$$

while the electron Compton length defines the corresponding electron-sector length scale. Since the photomagnetic activation coordinate is built from the electron-sector mass-to-magnetic-charge ratio,

$$\text{mchg} = \frac{m_{\text{e}}}{{e_{\text{emax}}}^2},$$

the natural projection length for electron activation is λ_C. In this sense, qild is the electron-sector length projection of qpmd.

3 QMU Thermal Regime Coordinate

The measured hot-electron energy E_h defines the QMU electron thermal fraction

$$\Theta_e = \frac{E_h}{m_{\text{e}}\,c^2}.$$

Since

$$m_{\mathrm{e}}\, c^2 = 0.51099895\,\mathrm{MeV},$$

the dimensionless regime coordinate is

$$\eta_q = \Theta_e = \frac{E_h}{0.51099895\,\mathrm{MeV}}.$$

In the first stage of the investigation, this coordinate is computed from measured hot-electron energy. In the predictive stage, however, η_q becomes the output to be predicted.

The wavelength-projected empirical coordinate is

$$q_T^* = \Theta_e \lambda_L.$$

The full QMU bridge from photomagnetic activation density to illumination behavior is

$$q_T = \Theta_e \frac{\mathrm{mchg}}{\mathrm{ligt}_L} = \Theta_e \frac{m_{\mathrm{e}}}{{e_{\mathrm{emax}}}^2 \mathrm{ligt}_L}.$$

Using

$$\mathrm{ligt}_L = \mathrm{phtn} f_L = \mathrm{angm} c f_L = \frac{\mathrm{angm} c^2}{\lambda_L}, \qquad {e_{\mathrm{emax}}}^2 = \mathrm{angm} C d,$$

this becomes

$$q_T = \frac{\Theta_e m_{\mathrm{e}} \lambda_L}{\mathrm{angm}^2 C d\, c^2}.$$

Holding the dimensional QMU constants fixed for empirical comparison gives

$$q_T^* = \Theta_e \lambda_L.$$

This coordinate does not replace Θ_e. It asks whether the electron rest-energy fraction acquires additional organizational meaning when projected through laser wavelength.

4 From Diagnostic Coordinate to Forward Prediction

The first diagnostic relation,

$$q_T^* = \Theta_e \lambda_L,$$

cannot by itself predict hot-electron energy because it contains

$$\Theta_e = \frac{E_h}{m_{\mathrm{e}}\, c^2}.$$

A forward prediction requires an equation of the form

$$\Theta_{e,\mathrm{pred}} = F_{\mathrm{QMU}}(I_L, \lambda_L, \tau_L, L_p, \mathrm{target}).$$

The simplest QMU-native predictive structure uses dimensionless laser-plasma inputs:

$$I_{18} \lambda_L^2,$$

$$\frac{c\tau_L}{\lambda_L},$$

and

$$\frac{L_p}{\lambda_L}.$$

Here I_{18} is laser intensity in units of $10^{18}\,\mathrm{W\,cm^{-2}}$, λ_L is the laser wavelength in micrometers, τ_L is the pulse duration, and L_p is the pre-plasma scale length. The conventional units enter only as database input coordinates; the fitted variables are the dimensionless QMU-normalized combinations $I_{18}\lambda_L^2$, $c\tau_L/\lambda_L$, and L_p/λ_L.

The forward QMU model tested in this paper is

$$\eta_{q,\mathrm{pred}} = A\left(I_{18}\lambda_L^2\right)^p \left(\frac{c\tau_L}{\lambda_L}\right)^s \left(\frac{L_p}{\lambda_L}\right)^r.$$

The corresponding hot-electron energy prediction is

$$E_{h,\mathrm{pred}} = m_\mathrm{e}\, c^2\, \eta_{q,\mathrm{pred}}.$$

5 Database and Data Classes

The analysis uses an expanded hot-electron workbook associated with the Rusby et al. electron-temperature meta-analysis. The present work builds upon the largest presently available meta-analysis of hot-electron temperatures derived from experiments and simulations of laser–solid interactions Rusby et al. [2024]. The database includes electron-temperature measurements, x-ray-inferred temperatures, simulations, and supplemental entries. The review describes the dataset as the largest collected electron-temperature dataset from high-intensity laser-solid experimental measurements and particle-in-cell simulations known to the author.

The present QMU analysis uses 555 usable records after parsing the available workbook sheets. The data classes are:

Electron measurements,

x-ray measurements,

simulations,

and

supplemental entries.

The main fields used are:

$$\lambda_L, \quad I_L, \quad \tau_L, \quad L_p, \quad E_h.$$

For each usable row, the following QMU-derived quantities were computed:

$$I_{18}\lambda_L^2,$$

$$\frac{c\tau_L}{\lambda_L},$$

$$\frac{L_p}{\lambda_L},$$
$$\eta_q = \Theta_e,$$
$$q_T^* = \Theta_e \lambda_L.$$

6 Model Family

Four nested QMU models were tested.

The first model uses only wavelength-projected intensity:

$$\eta_{q,\mathrm{pred}} = A \left(I_{18} \lambda_L^2 \right)^p .$$

The second model adds pulse duration in optical cycles:

$$\eta_{q,\mathrm{pred}} = A \left(I_{18} \lambda_L^2 \right)^p \left(\frac{c\tau_L}{\lambda_L} \right)^s .$$

The third model adds pre-plasma scale length:

$$\eta_{q,\mathrm{pred}} = A \left(I_{18} \lambda_L^2 \right)^p \left(\frac{L_p}{\lambda_L} \right)^r .$$

The fourth model uses all three QMU coordinates:

$$\eta_{q,\mathrm{pred}} = A \left(I_{18} \lambda_L^2 \right)^p \left(\frac{c\tau_L}{\lambda_L} \right)^s \left(\frac{L_p}{\lambda_L} \right)^r .$$

The logarithmic form fitted to the data is

$$\ln \eta_q = \ln A + p \ln\left(I_{18} \lambda_L^2 \right) + s \ln\left(\frac{c\tau_L}{\lambda_L} \right) + r \ln\left(\frac{L_p}{\lambda_L} \right).$$

The fits were performed by ordinary least squares in logarithmic space. Predictive performance was evaluated by five-fold cross-validation using the same feature set for each fold. The reported $R^2_{\log}$ values are computed from the cross-validated logarithmic predictions. The coefficient uncertainties reported below are one-standard-error estimates from the log-linear regression covariance matrix for the fitted model. These uncertainties quantify the stability of the empirical exponents within the present dataset; they do not represent a first-principles derivation of those exponents.

7 Global Results

The full QMU model for all available rows with intensity, wavelength, pulse duration, and scale length is

$$\eta_{q,\mathrm{pred}} = 0.197511 \left(I_{18} \lambda_L^2 \right)^{0.508959} \left(\frac{c\tau_L}{\lambda_L} \right)^{0.268821} \left(\frac{L_p}{\lambda_L} \right)^{0.275917} .$$

The one-standard-error coefficient estimates are

$$A = 0.197511 \pm 0.025330,$$

$$p = 0.508959 \pm 0.014148,$$

$$s = 0.268821 \pm 0.021134,$$

$$r = 0.275917 \pm 0.022377.$$

For the full model, the global cross-validated result is:

$$R^2_{\log} = 0.828899.$$

The error statistics are:

$$\mathrm{RMSE} = 3.676205\,\mathrm{MeV},$$

$$\mathrm{MAE} = 1.978955\,\mathrm{MeV}.$$

The prediction falls within a factor of two for

$$86.6906\%$$

of the usable full-model rows, and within a factor of three for

$$96.7626\%.$$

Table 2: Global QMU model performance.

Model	N	$R^2_{\log}$	RMSE MeV	MAE MeV	Factor 2
$A(I_{18}\lambda_L^2)^p$	555	0.549	5.917	3.456	0.452
$A(I_{18}\lambda_L^2)^p(c\tau_L/\lambda_L)^s$	478	0.686	5.039	2.944	0.561
$A(I_{18}\lambda_L^2)^p(L_p/\lambda_L)^r$	283	0.725	4.933	2.727	0.767
Full QMU model	278	0.829	3.676	1.979	0.867

The first row of Table 2 is intentionally retained as the single-coordinate baseline. It is the closest comparison to a wavelength-projected ponderomotive-style scaling because it uses only $I_{18}\lambda_L^2$. The purpose of the added QMU coordinates is not to replace that scaling, but to test whether QMU-normalized interaction duration and scale length account for additional structure already present in the measurements. The increase from $R^2_{\log} = 0.549$ for the single-coordinate model to $R^2_{\log} = 0.829$ for the full QMU model shows that the electron activation regime is not determined by intensity projection alone in this database.

8 Class-Specific Results

Because electron measurements, x-ray measurements, and simulations are not identical measurement classes, they should not be forced into a single physical interpretation. Each class measures hot-electron behavior through a different observational path.

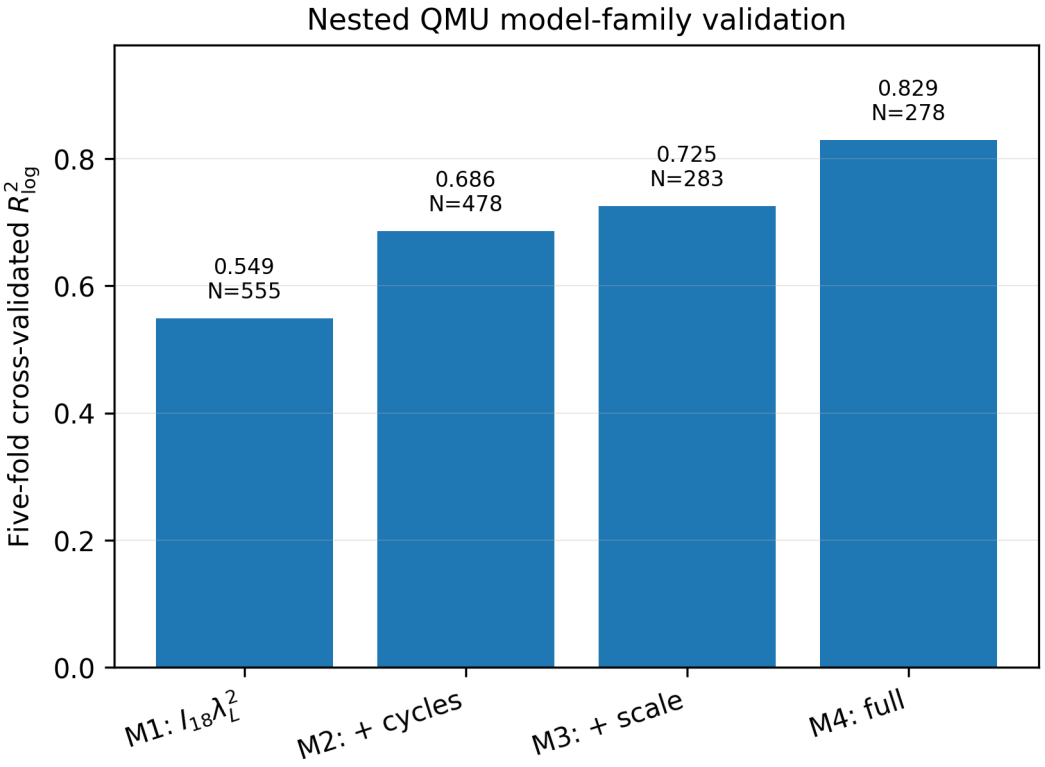

Figure 1: Nested QMU model-family validation. The single-coordinate model uses only wavelength-projected intensity, $I_{18}\lambda_L^2$. Adding pulse duration in optical cycles and pre-plasma scale length in laser wavelengths progressively increases the cross-validated logarithmic agreement with the measured electron activation coordinate, η_q.

For electron measurements, the full model gives:

$$R^2_{\log} = 0.759342.$$

The electron-measurement exponents are

$$p = 0.449169 \pm 0.023552, \quad s = 0.237943 \pm 0.038063, \quad r = 0.292638 \pm 0.047174.$$

For x-ray measurements, the pulse-duration model already gives:

$$R^2_{\log} = 0.918518.$$

For that x-ray model,

$$p = 0.590366 \pm 0.022978, \quad s = 0.121280 \pm 0.043432.$$

The full three-coordinate model is not emphasized for x-ray data because the available full-model x-ray subset is too small to support a meaningful three-parameter fit.

For simulations, the full model gives:

$$R^2_{\log} = 0.908.$$

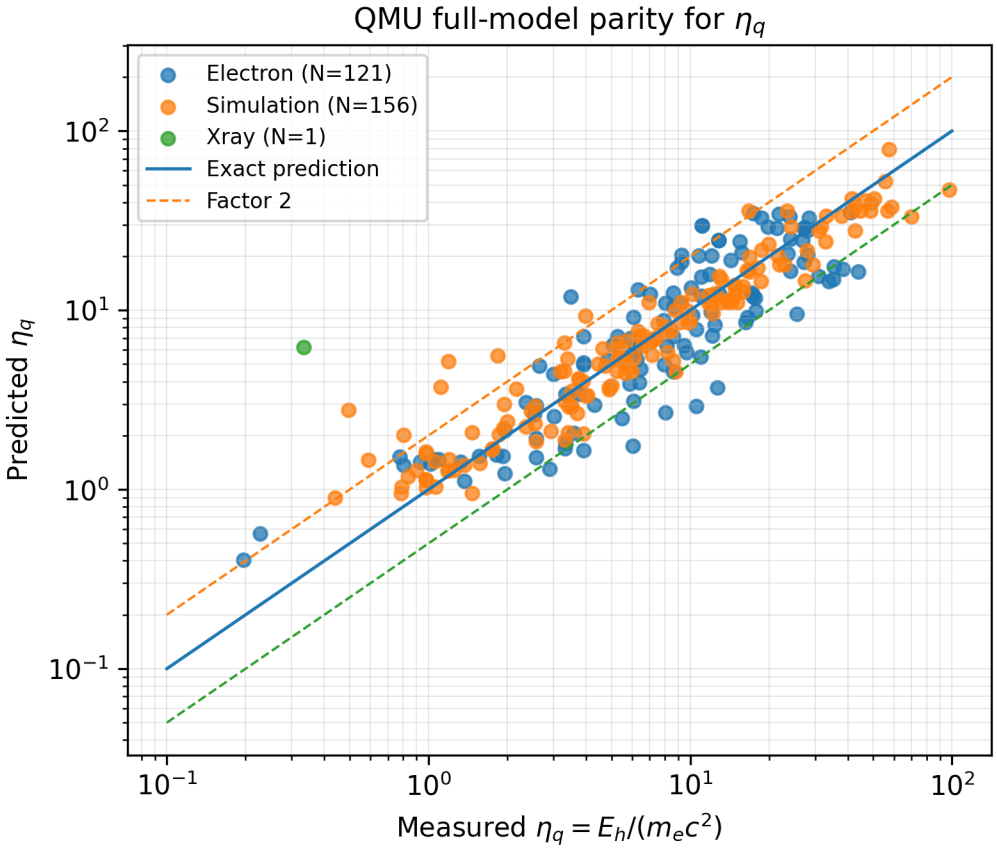

Figure 2: Predicted versus measured QMU electron activation coordinate for the full QMU model. The diagonal line indicates exact agreement, while the dashed lines indicate a factor-of-two envelope. The plot is shown in the dimensionless QMU coordinate $\eta_q = E_h/(m_e\, c^2)$ rather than in ordinary hot-electron temperature units.

The simulation exponents are

$$p = 0.555348 \pm 0.013998, \quad s = 0.268834 \pm 0.020445, \quad r = 0.275765 \pm 0.019463.$$

These class-specific results show that the QMU coordinate system is not merely fitting one homogeneous subset. It recovers substantial structure across measurement and simulation classes while also showing that different measurement paths should not be forced into a single artificial interpretation.

Table 3: Class-specific QMU performance for selected models.

Class	Model	N	$R^2_{\log}$	RMSE MeV	Factor 2
Electron	Full QMU model	121	0.759	3.524	0.835
X-ray	$I\lambda^2$ plus cycles	59	0.919	0.423	0.915
Simulation	Full QMU model	146	0.908	3.328	0.911

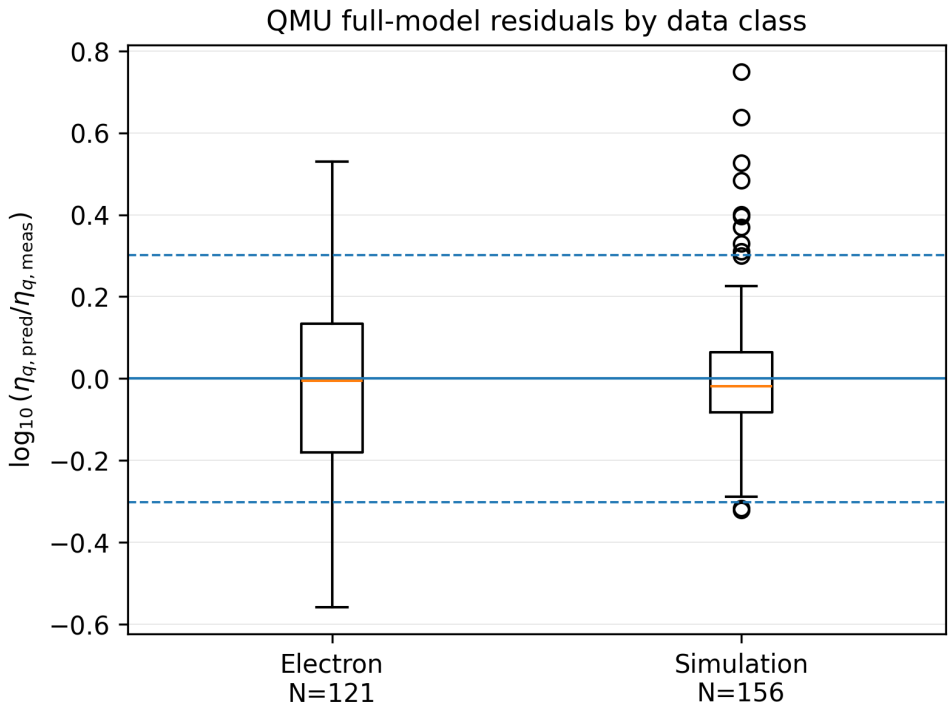

Figure 3: Full-model residual structure by data class. The plotted quantity is $\log_{10}(\eta_{q,\mathrm{pred}}/\eta_{q,\mathrm{meas}})$. The central horizontal line marks exact agreement and the dashed lines mark a factor-of-two envelope. This figure shows that the QMU forward law recovers structure across measurement and simulation classes while preserving class-specific residual behavior.

9 Interpretation of the Exponents

The fitted exponents are physically meaningful in QMU terms.

The global full-model intensity-wavelength exponent is

$$p = 0.508959.$$

The fitted exponent is notably close to the familiar square-root dependence associated with ponderomotive scaling laws Wilks et al. [1992], Kruer [1988]. This is close to a square-root response in the wavelength-projected intensity coordinate:

$$\eta_q \propto (I_{18}\lambda_L^2)^{1/2}.$$

The pulse-cycle exponent is

$$s = 0.268821,$$

showing that longer interaction duration, measured in optical cycles, increases the predicted electron activation fraction.

The scale-length exponent is

$$r = 0.275917,$$

showing that pre-plasma scale length, measured in laser wavelengths, contributes directly to the QMU activation regime.

Thus the fitted law can be read as:

$$\eta_q \sim \text{wavelength-projected intensity}^{1/2} \times \text{cycle duration}^{0.27} \times \text{scale-length projection}^{0.28}.$$

This is consistent with the interpretation of qild as a spatially projected illumination coordinate. The scale-length term is not incidental; it is the clearest indication that luminous activation depends upon spatial organization.

10 Illumination Density and Regime Boundaries

The earlier electron-only database produced tentative empirical q_T^* boundaries near

$$0.464\,\mu\text{m}$$

and

$$5.354\,\mu\text{m}.$$

After expansion to the full 555-row database, the global tertile boundaries shifted to

$$2.44045\,\mu\text{m}$$

and

$$8.61403\,\mu\text{m}.$$

The database consists of electron measurements, x-ray measurements, simulations, and supplemental records compiled in the recent hot-electron meta-analysis of laser–solid interactions Rusby et al. [2024].

Converted to QMU Compton-length counts, these are

$$2.44045\,\mu\text{m} = 1.00583 \times 10^6\,\lambda_C,$$

and

$$8.61403\,\mu\text{m} = 3.55026 \times 10^6\,\lambda_C.$$

Because the earlier boundaries do not survive as universal boundaries in the expanded dataset, they should not be interpreted as fundamental QMU constants. Instead, the present result is more conservative: illumination-density bands are empirical, class-dependent structures. Stable QMU-geometric interpretation should only be attempted after the same boundaries recur across independent, wavelength-diverse datasets.

11 Validation Standard

The validation standard in this paper is not competitive superiority over existing laser-plasma models. The validation standard is whether QMU-native coordinates can predict the measured hot-electron regime using QMU-relevant inputs.

The answer from the present dataset is affirmative in first-pass form:

$$\eta_{q,\mathrm{pred}} = F_{\mathrm{QMU}}\left(I_{18}\lambda_L^2, \frac{c\tau_L}{\lambda_L}, \frac{L_p}{\lambda_L}\right)$$

reproduces a large fraction of the measured hot-electron structure.

The result is especially important because η_q is not a conventional fitted temperature label. It is the electron rest-energy fraction:

$$\eta_q = \frac{E_h}{m_{\mathrm{e}}\, c^2}.$$

Therefore, the prediction is made directly in QMU regime units.

12 Limitations

Several limitations remain.

First, the full model uses fewer rows than the simplest model because pre-plasma scale length is missing for many entries.

Second, the dataset is dominated by common high-intensity laser wavelengths near one micrometer. Additional data at

$$0.35\,\mu\mathrm{m}, \quad 0.53\,\mu\mathrm{m}, \quad 0.8\,\mu\mathrm{m}, \quad 1.05\,\mu\mathrm{m}, \quad 10.6\,\mu\mathrm{m}$$

would provide a stronger test of wavelength projection.

Third, target material and target geometry were not yet included in the predictive model. These may be essential for structured targets such as compound parabolic concentrators, micro-wires, foams, cones, and layered targets. The compound parabolic concentrator experiments provide a useful example of enhanced electron production occurring within a distinct illumination-density regime Rusby et al. [2021].

Fourth, the present model is empirical. It identifies a QMU-native forward law, but it does not yet derive the exponents from first principles.

13 Future Work

The next stage is to extend the QMU predictive law by adding target and coupling observables:

$$Z, \quad \rho, \quad A_L, \quad B_{\mathrm{self}}, \quad Y_X, \quad E_{i,\mathrm{max}}.$$

The most important question is whether qild predicts coupling observables beyond hot-electron temperature:

$$\text{qild} \leftrightarrow \text{absorption efficiency},$$

$$\text{qild} \leftrightarrow \text{self-generated magnetic fields},$$

$$\text{qild} \leftrightarrow \text{x-ray yield},$$

$$\text{qild} \leftrightarrow \text{ion acceleration}.$$

Because self-generated magnetic fields influence electron transport and hotspot evolution, quantum illumination density may ultimately prove useful as an organizational coordinate for magnetized coupling phenomena Sadler et al. [2022].

A subsequent paper should therefore test whether the predicted QMU activation fraction

$$\eta_{q,\mathrm{pred}}$$

and the projected illumination coordinate

$$q^{*}_{T,\mathrm{pred}} = \lambda_L \eta_{q,\mathrm{pred}}$$

organize these secondary observables.

14 Conclusion

This paper introduces Quantum Illumination Density,

$$\mathrm{qild} = \lambda_C \, \mathrm{qpmd},$$

as the characteristic-length projection of Quantum Photomagnetic Density. The distinction developed here is:

$$\begin{aligned} \mathrm{qpmd}: &\quad \text{mass-to-magnetic-charge activation per luminous condition,} \\ \mathrm{qild}: &\quad \text{characteristic-length projection of that activation.} \end{aligned}$$

The investigation advances beyond diagnostic conversion by testing a forward QMU prediction law:

$$\eta_{q,\mathrm{pred}} = A \left(I_{18}\lambda_L^2\right)^{p} \left(\frac{c\tau_L}{\lambda_L}\right)^{s} \left(\frac{L_p}{\lambda_L}\right)^{r}.$$

For the expanded Rusby-derived database, the full model reproduces measured hot-electron structure with

$$R^2_{\log} = 0.829$$

globally where all inputs are available, with strong class-specific performance for electron measurements, x-ray measurements, and simulations.

This result gives qild a genuine scientific path. It is not merely a new name for hot-electron temperature. It is part of a QMU predictive structure in which electron activation is expressed through wavelength-projected intensity, optical-cycle duration, and scale-length projection. The data therefore support the use of quantum illumination density as the next operational QMU research tool after qpmd.

Supplemental Workbook and Figures

The accompanying Zenodo package includes a fully populated companion workbook containing the expanded Rusby-derived hot-electron database together with all QMU-derived calculations used

in this paper. The workbook preserves the processed prediction data, fitted model coefficients, cross-validated performance summaries, class-specific analyses, empirical boundary calculations, and explanatory notes required to reproduce the reported results.

The principal computed columns are:

$$\Theta_e, \quad q_T^*, \quad I_{18}\lambda_L^2, \quad \frac{c\tau_L}{\lambda_L}, \quad \frac{L_p}{\lambda_L}, \quad \eta_q, \quad \eta_{q,\mathrm{pred}}, \quad E_{h,\mathrm{pred}}.$$

The Zenodo package also includes the figures used in the present paper. These comprise the nested QMU model-family validation plot, the predicted-versus-measured parity plot for the electron activation coordinate, the residual distributions by data class, and the distribution of wavelength-projected thermal activation expressed as QMU Compton-length counts. Together, the workbook and figures provide a complete computational record of the present analysis and permit independent verification of all tables, figures, and derived quantities reported herein.

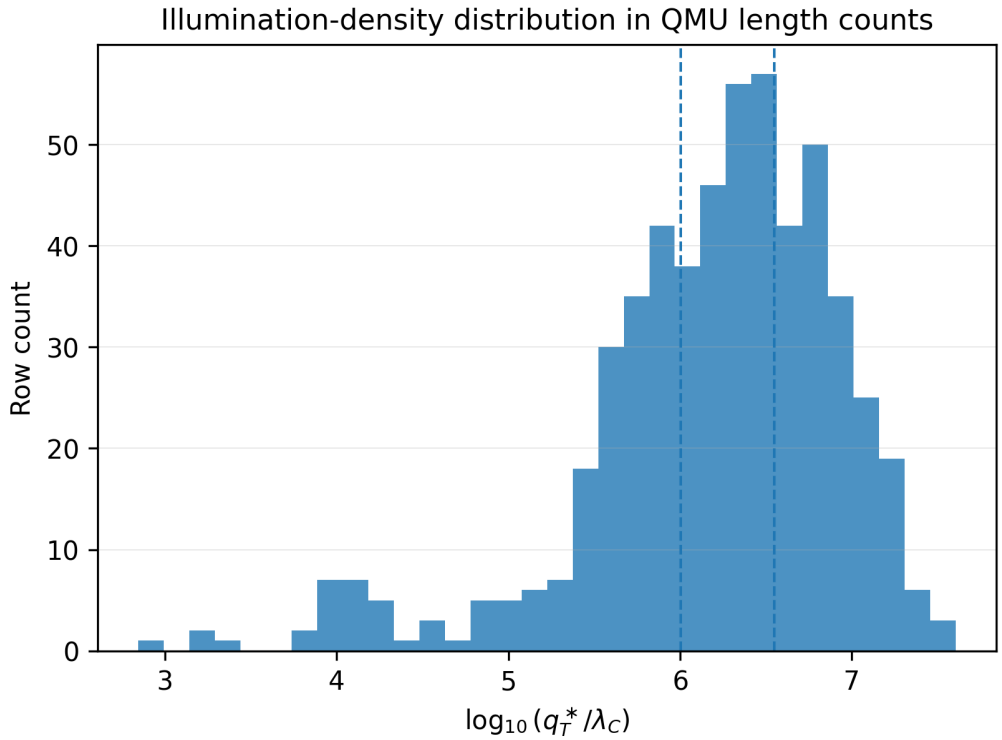

Figure 4: Distribution of measured wavelength-projected thermal activation, expressed as QMU Compton-length counts q_T^*/λ_C. The dashed vertical lines mark empirical tertile boundaries for the expanded database. These boundaries are reported as data-emergent bands only, not as fundamental QMU constants.

Data and Reproducibility

The calculations in this paper were performed on the expanded hot-electron workbook derived from the Rusby et al. dataset. The QMU analysis workbook generated for this paper contains the

processed prediction data, fitted model coefficients, cross-validated performance summaries, and interpretation notes. The primary computed columns are:

$$\Theta_e, \quad q_T^*, \quad I_{18}\lambda_L^2, \quad \frac{c\tau_L}{\lambda_L}, \quad \frac{L_p}{\lambda_L}, \quad E_{h,\mathrm{pred}}.$$

Acknowledgments

The Quantum AetherDynamics Institute (QADI) is a private 501(c)(3) research institute developing the Aether Physics Model (APM) and Quantum Measurement Units (QMU) Thomson III [2025]. Publications and data are archived with DOIs in the AetherPhysics Zenodo community: zenodo.org/communities/aetherphysics.

References

William L. Kruer. *The Physics of Laser Plasma Interactions*, volume 73 of *Frontiers in Physics*. Addison-Wesley Publishing Company, Redwood City, California, 1988. ISBN 9780201156720. URL https://www.worldcat.org/oclc/859669066.

D. R. Rusby, N. Lemos, H. Chen, A. Kemp, A. Longman, S. Kerr, A. Aghedo, S. C. Wilks, G. J. Williams, J. Bude, and A. J. Mackinnon. Enhancements in laser-generated hot-electron production via compound parabolic concentrator targets. *Physical Review E*, 103:053207, 2021. doi: 10.1103/PhysRevE.103.053207. URL https://doi.org/10.1103/PhysRevE.103.053207.

D. R. Rusby, A. J. Kemp, S. C. Wilks, K. G. Miller, M. Sherlock, H. Chen, R. A. Simpson, D. A. Mariscal, K. Swanson, B. Z. Djordjevic, A. J. Link, G. J. Williams, and A. J. Mackinnon. Review and meta-analysis of electron temperatures from high-intensity laser–solid interactions. *Physics of Plasmas*, 31(4):040503, 2024. doi: 10.1063/5.0197279. URL https://doi.org/10.1063/5.0197279.

J. D. Sadler, C. A. Walsh, H. Li, et al. Role of self-generated magnetic fields in the inertial fusion hotspot. *Physics of Plasmas*, 29(7):072701, 2022. doi: 10.1063/5.0094057. URL https://doi.org/10.1063/5.0094057.

David W. Thomson. Photomagnetic Activation Density in Laser-Plasma Data: A QMU Demonstration of qpmd, June 2026. URL https://doi.org/10.5281/zenodo.20971999.

David W. Thomson III. A novel interpretation of the ideal gas law and its relation to black body radiation using the aether physics model, oct 2024. URL https://doi.org/10.13140/RG.2.2.30228.31368. License: CC BY-ND 4.0.

David W. Thomson III. Quantum aetherdynamics institute (qadi): Community doi overview and citation guide. Zenodo, 2025. URL https://doi.org/10.5281/zenodo.17479314.

E. Tiesinga, P. J. Mohr, D. B. Newell, and B. N. Taylor. Codata recommended values of the fundamental physical constants: 2022. *Reviews of Modern Physics*, 95:025010, 2023. doi: 10.1103/RevModPhys.95.025010.

S. C. Wilks, W. L. Kruer, M. Tabak, and A. B. Langdon. Absorption of ultra-intense laser pulses. *Physical Review Letters*, 69(9):1383–1386, 1992. doi: 10.1103/PhysRevLett.69.1383. URL https://doi.org/10.1103/PhysRevLett.69.1383.

S. C. Wilks, A. B. Langdon, T. E. Cowan, M. Roth, M. Singh, S. Hatchett, M. H. Key, D. Pennington, A. MacKinnon, and R. A. Snavely. Energetic proton generation in ultra-intense laser–solid interactions. *Physics of Plasmas*, 8(2):542–549, 2001. doi: 10.1063/1.1333697. URL https://doi.org/10.1063/1.1333697.